Journal of Alloys and Compounds 995 (2024) 174845

Contents lists available at ScienceDirect

Journal of Alloys and Compounds

journal homepage: www.elsevier.com/locate/jalcom

Green biomediated synthesis of anodized WO_3 nanocatalysts using *Melia azedarach* leaves extract for the energetic transition: Solar hydrogen and Li-ion batteries

Ramón M. Fernández-Domene [a,*], Benjamin Solsona [a], María Erans [a], Encarna Blasco-Tamarit [b], Rita Sánchez-Tovar [a]

[a] IQCATAL Group (Heterogeneous Catalysis), Chemical Engineering Department (ETSE), Universitat de València, Av. Universitat s/n, Burjassot-Valencia 46100, Spain
[b] Instituto Universitario de Seguridad Industrial, Radiofísica y Medioambiental (ISIRYM), Universitat Politècnica de València, Camino de Vera s/n, Valencia 46022, Spain

ARTICLE INFO

Keywords:
Green chemistry
Nanotechnology
Plant extract
Solar hydrogen
Photoelectrocatalysis
Li-ion batteries

ABSTRACT

This study reports the bio-mediated synthesis of tungsten trioxide nanostructures from aqueous extracts of *Melia azedarach* (L.) dry leaves. The synthesis was carried out by electrochemical anodization of tungsten foils in the presence of different volume percentages of leaves extracts. These nanostructures were afterwards completely characterized by Field-Emission Scanning Electron Microscopy (FESEM), X-Ray Diffraction (XRD), High-Resolution Transmission Electron Microscopy (HR-TEM), impedance measurements, linear sweep voltammetry in the presence of simulated solar light and UV-Vis spectroscopy. Finally, these nanoelectrodes were used as (photo)electrocatalysts in the photoelectrochemical water splitting process to obtain green hydrogen and as anodes in Li-ion rechargeable batteries. Nanostructures fabricated with 5% M. azedarach leaves extract provided the best (photo)electrocatalytic behavior for both applications, since in that biogenic electrolyte, thin nanorods arranged in very porous and spongy layers were formed. Therefore, the significant increase in specific surface area found for nanostructures fabricated following this green route, in comparison with the blank sample (i.e., nanostructure formed following a non-green route), was essential to enhance their performance as promising efficient (photo)electrocatalysts.

1. Introduction

Approximately 82% of the world's energy consumption stems from non-renewable fossil fuel sources [1]. This heightened demand for energy, which has been on a steady rise since the dawn of the industrial revolution, has resulted in increased emissions of greenhouse gases, primarily carbon dioxide (CO_2), into the Earth's atmosphere. It is widely acknowledged that the escalating concentration of greenhouse gases is the principal driver of global warming and, consequently, climate change [2–4]. In this context, hydrogen emerges as a viable, clean, and sustainable energy solution. Nevertheless, the transition from well-established fossil fuel technologies to efficient, cost-effective, and, notably, environmentally friendly hydrogen production methods poses a considerable challenge [2–7]. As a response, there is a growing push for renewable (green) hydrogen production techniques, with one of the most promising approaches being the utilization of photoelectrochemical (PEC) water splitting, also known as photoelectrolysis, employing nanostructured electrodes [6,8–11]. This innovative process harnesses solar energy directly, using semiconductors to split water molecules into hydrogen and oxygen at separate electrodes. While PEC water splitting remains a technology in the developmental stages, requiring further research and refinement, its distinct advantages over alternative hydrogen production methods and minimal environmental footprint make it a very promising technology for the future [6, 8–11].

Nanotechnology also holds significant promise in another domain: the advancement of alternative energy storage systems [12–19]. With the widespread use of portable electronic devices and the growing adoption of electric vehicles, the imperative for the creation of clean and highly efficient electric energy storage solutions has become increasingly evident. In this context, electrochemical batteries have assumed a pivotal role. Among the various types of rechargeable or secondary

* Corresponding author.
E-mail address: ramon.fernandez@uv.es (R.M. Fernández-Domene).

https://doi.org/10.1016/j.jallcom.2024.174845
Received 21 March 2024; Received in revised form 9 May 2024; Accepted 12 May 2024
Available online 13 May 2024

batteries, those employing lithium-ion (Li^+) insertion/extraction processes have emerged as the most advanced energy storage mechanisms thus far [12–24]. However, these batteries deal with several challenges concerning the kinetics of the process, long-term stability, and safety aspects. Consequently, it is essential to persist in the pursuit of innovations within this domain, particularly in the development of novel electrode materials that can substantially enhance battery performance. Presently, nanotechnology stands as a prominent opportunity in the quest for novel battery electrode materials, particularly those based on metal oxides [13,15,17,20,21]. Hence, oxides such as TiO_2, NiO, CuO, Fe_2O_3, SnO_2, WO_3, Co_3O_4, etc. are being investigated due to their potentialities as substitutes for graphite as negative electrode materials (anodes on discharge), such as high specific capacity values, stability, avoidance of metallic lithium formation and high conductivities and lithium ion diffusivities due to nanostructured morphologies [13,15,17,20,21]. These metal oxides can interact with lithium ions following two general mechanisms: (1) insertion or intercalation reaction, in which Li^+ reversibly intercalates within the oxide lattice without structural transformations, and (2) conversion reaction between Li^+ and the oxide to form Li_2O [15,20]. Depending on the nature of the main reaction between lithium ions and the metal oxide, and on the properties, morphology and size of the electrode materials, different behaviors and battery performances could be achieved.

There is, therefore, a necessity for developing new electrode nanostructured materials based on transition metal oxides for rechargeable LIBs with improved insertion/extraction properties and with long lifespans.

Nanostructures of tungsten trioxide, WO_3, are being increasingly used as (photo)electrodes due to its suitable band-gap value (~2.6 eV), excellent chemical stability in many electrolytes (especially acidic ones) and good electrical and electrochemical properties [25–29]. Numerous synthesis methodologies have been reported, such as sol-gel processes, hydrothermal and solvothermal methods or deposition processes. In most cases, these procedures involve the use of hazardous and/or expensive chemicals and solvents, long reaction times and high energy requirements, with the subsequent negative environmental and economic impact. Very recent strategies have been based on the use of biogenic entities in the reaction media, such as plant extracts or microorganisms, which are considered as ideal green reagents because they are perfectly safe, cheap and environmentally-friendly [30–34]. In particular, plant extracts are favored over alternative biogenic reagents due to their ready availability and ease of safe handling [35–37]. Moreover, the presence of a rich variety of organic molecules in these extracts (polyphenols, flavonoids, tannins, etc.), which are capable of act as metal-complexing (or capping) agents [32,36,38–40], opens a wide opportunity to control the nanostructures reaction mechanisms and, therefore, to adjust their morphology, size and properties, following at the same time the principles of green chemistry.

Most of the published studies on nanomaterials biosynthesis deal with the fabrication of metal (Ag, Cu, etc.) nanoparticles [30,40–44], although some of these methods have also been used to obtain metal oxides nanoparticles, especially ZnO and TiO_2 [35,37,38,45–53]. Nevertheless, no studies have been found in which biosynthetic routes using electrochemical methods, such as anodization, are employed. Anodization is one of the most fast and simple methods to fabricate metal oxides nanostructures. This technique offers great controllability, since the size and morphology of these nanostructures can be regulated by controlling parameters such as the applied potential, time, electrolyte composition, hydrodynamic conditions, etc. [29,54–56].

Therefore, the primary motivation behind this study stems from the noticeable absence of literature on synthesizing metal oxide nanostructures, particularly WO_3, via anodization in environmentally friendly electrolytes in the presence of biological complexing agents derived from plant extracts. This approach has the potential to finely tune the morphology and dimensions of the resulting nanostructures. In the present work, leaves extracts of Melia azedarach L. (Meliaceae) have been used as main electrolyte reagents to obtain high performance WO_3 nanostructures by electrochemical anodization. This particular tree has been chosen for its extensive diversity, notably found throughout Spain as an attractive urban tree, and its exceptional composition, since its leaves are rich in various adequate phytochemicals for nanomaterials synthesis, including polyphenols, flavonoids, and tannins [38,39,57–60]. In fact, these biomolecules and metabolites have been studied for having antibiotic, antioxidant, anti-inflammatory and anticancer activity, among others [35,39,41,57,59]. Hence, a complete investigation comparing the influence of the extract percentage on the morphological, electrochemical and photoelectrochemical properties of the obtained WO_3 nanostructures is presented in this work. Moreover, the formation mechanism of these nanostructures has been studied in depth in the absence and in the presence of these biomolecules.

The green synthesis method reported here, which uses, on the one hand, biological molecules in the electrolyte composition and, on the other hand, the complex chemistry of tungsten with the aim of producing innovative and high aspect ratio nanostructures, represents a simple, non-expensive and environmentally friendly approach to control and adjust the morphology and size of these nanostructures and, therefore, their fundamental properties. Besides, the (photo)electrochemical applications of these bio-synthesized WO_3 nanostructures will contribute to provide solutions to the challenges associated with the energetic transition, such as the production of green hydrogen and the fabrication of efficient and reliable energy storage systems.

2. Materials and methods

2.1. Synthesis of WO_3 nanostructures

The leaves of M. azedarach were randomly sampled from several mature trees from the surroundings of the Burjassot Campus of the University of Valencia (Spain). Fresh leaves were rinsed with tap and distilled water and subsequently air-dried indoors for 1 week, at room temperature. The extracts were obtained from dried leaves, by mixing 15 g of material with 150 mL of distilled water at 60 ºC. The infusion was maintained at that temperature for 20 min. After that, the solution, once cooled, was filtered through filter paper and used to prepare the different reaction media.

Nanostructures of WO_3 were synthesized by subjecting tungsten foils (1,3 cm^2 of exposed area) to an anodization process with a cell potential of 20 V, for 4 h. A platinum foil served as the cathode within the cell. The anodization process employed an aqueous electrolyte composed of 1.5 M methanesulfonic acid (MSA) with varying proportions of M. azedarach leaves extract (from 0% to 10%, in volume), at a temperature of 50°C. MSA was selected for two reasons: (1) because in a previous study [61], it was observed that WO_3 nanorods formed in the presence of MSA provided enhanced photoelectrocatalytic performance than those anodized with other strong acid such as sulfuric acid, and (2) because MSA has been found to be less toxic than other strong acids, it has no permissive exposure limit (OSHA PEL) due to the absence of risky volatile chemicals under normal conditions and it is easily biodegradable to yield SO_4^{2-}, CO_2, water and biomass, since MSA is part of the natural geochemical cycle of sulfur [62,63]. Anodization was performed under controlled hydrodynamic conditions, by means of a Rotating Disk Electrode (RDE) set a constant rotation speed of 750 rpm. Following anodization, a thermal treatment (annealing) was carried out in a tubular oven at 600°C for 4 h in an air atmosphere to obtain crystalline WO_3 nanostructures.

2.2. Morphological and structural characterization: FESEM, XRD and HRTEM

A Field Emission Scanning Electronic Microscope (Hitachi S4800), at an acceleration potential of 5 kV, was used to study the morphology and size of the WO_3 nanostructures.

X-Ray diffraction analyses (XRD) were performed to investigate the crystallinity of the WO_3 samples. A D8AVANCE diffractometer (Bruker) equipped with a monochromatic Cu Kα1 source was used.

Structural and morphological characterization of the samples was also undertaken by Transmission Electron Microscopy (TEM) and high resolution TEM (HRTEM). FEI Field Emission Gun (FEG) TECNAI G2 F20 S-TWIN microscopy working at 200 kV was used for the present study. Before the introduction of the samples in the microscopy, they were sonicated for 5 min in pure ethanol. A drop of the resulting suspension was deposited onto a holey carbon film supported on a copper grid and, finally, dried.

2.3. (Photo)electrochemical characterization: impedance measurements and photocurrent density vs potential curves

Electrochemical characterization of the WO_3 nanostructures was conducted through impedance measurements, performing Electrochemical Impedance Spectroscopy (EIS) and Mott-Schottky (MS) analyses. All electrochemical tests were carried out using a three-electrode cell with the nanostructures acting as working electrodes, a silver/silver chloride (3 M KCl) electrode was the reference electrode and a platinum tip served as counterelectrode. Measurements were performed with a PalmSens4 potentiostat and 0.1 M H_2SO_4 was used as electrolyte. The sample area exposed to that electrolyte was 0.5 cm^2. For EIS, a constant potential of 1 V was selected with an amplitude of 10 mV, scanning the frequency from 100 kHz to 10 mHz. For MS analysis, a constant frequency of 5 kHz was used, while the potential was scanned from 1 V to 0.2 V at a rate of 50 mV/s.

For the photoelectrochemical characterization of the WO_3 nanostructures, the same experimental set-up was used, with the addition of a solar simulator with AM 1.5 conditions (100 mW/cm^2). Linear voltammetries to obtain photocurrent density – potential curves were conducted from 0.2 V to 1.05 V, by applying dark-light pulses (16 s in the dark followed by 4 s with illumination) while the potential was scanned.

Finally, UV–vis diffuse reflectance experiments were carried out within the 220–850 nm range using a Shimadzu spectrometer model UV-1800. The spectra shown has been obtained from WO3 samples prepared by anodization of metallic W in the absence or in the presence of different extract concentrations. The band gap energy values were obtained by extrapolating the linear fitted region at $[F(R(\infty))h\nu]^2 = 0$ in the plot of $[F(R(\infty))\ h\nu]$ versus $h\nu$.

2.4. Evaluation of WO_3 nanostructures as Li-ion battery anodes

WO_3 nanostructures were evaluated as anodes (negative electrodes) for Li-ion batteries. For that purpose, Swagelok-type cells were used, with WO_3 nanostructures acting as working electrodes and a metallic lithium foil acting as both the counter and the reference electrodes. Batteries were assembled inside an Ar-filled glove box, using 1 M $LiPF_6$ in ethylene carbonate/dimethyl carbonate/diethyl carbonate 1:1:1 (v/v/v) as electrolyte (Sigma-Aldrich) and a Whatman glass microfiber separator. After sealing the cells, they were cycled outside the glove box at room temperature, using a Biologic BCS-815 cyclic station. Galvanostatic charge/discharge curves were recorded at different cycling rates (from C/10–1 C, and returning to C/10) within a potential window between 1 V and 3.5 V vs Li/Li^+.

3. Results and discussion

3.1. Formation mechanism: current density transients during anodization

Fig. 1 shows the current density variation with time during anodization of the different nanostructures fabricated in the absence (blank) and in the presence of various amounts (in % V/V) of M. azedarach leaves extract. In all the curves, three different regions are discerned.

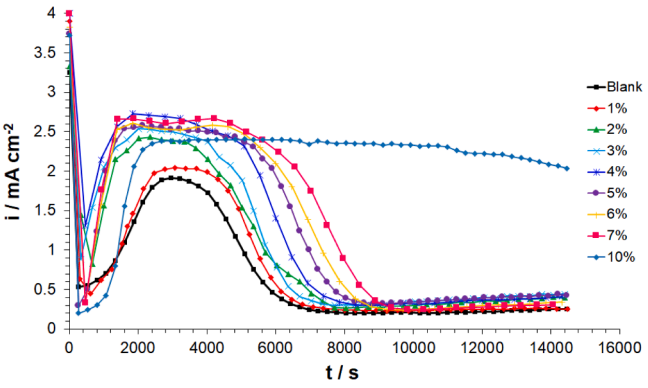

Fig. 1. Current density transient recorded during tungsten anodization for the different samples, fabricated without extract (blank) and with different extract (V/V) percentages.

The first region, which is the shortest one, consists of a sharp decrease in current density due to oxidation of the tungsten surface upon imposing a potential difference of 20 V. Hence, the compact WO_3 layer formed in this region obstructed charge transfer processes, resulting in a fast decrease of current density.

After that, the second region appears with a progressive increase in current density and a subsequent stabilization, due to the dissolution of the previously formed WO_3 compact layer. In the absence of M. azedarach extract (blank sample), this dissolution process was mediated by the high concentration of H^+ cations. As a result, tungsten soluble species (typically in the form of WO_2^{2+} species, or $[W(OH)_4(H_2O)_4]^{2+}$) were formed [55,64,65]. In the presence of M. azedarach extract, current density values in this second region increased with respect to the curve for the blank sample, and this current density rise began, in general, at shorter times as the extract concentration increased. These facts indicate that dissolution of the WO_3 compact layer took place faster when M. azedarach extract was present in the anodization electrolyte. It has been reported that M. azedarach extracts present numerous polyphenolic compounds in high concentrations (phenolic acids, flavonols, etc.), such as quercetin, kaempferol and derivatives of catechol, caffeic acid and ferulic acid, among others [39,57–60,66]. These phytochemicals have been reported to behave as ligation (complexing) agents of many metals, due to the different aromatic hydroxyl groups present in their molecules [31,39,67,68]. For example, a typical polyphenolic compound (flavonoid) such as quercetin (Fig. 2a) has three possible metal-complexation sites [67,68], where tungsten atoms can be strongly bound. Indeed, phenoxide groups promote the chelation of cations with high charge density [67], such as W^{6+}. Therefore, the presence of M. azedarach leaves extract promoted the dissolution of WO_3 through polyphenolic-induced polymerization of tungsten complex and soluble species, thus increasing current density in this second stage. In Fig. 2b, a scheme of a possible interaction between quercetin molecules and tungsten is presented, by way of illustration.

As these soluble species were formed, their concentration at the electrode/electrolyte interface grew and, when supersaturation conditions were reached, they precipitated in the form of hydrated tungsten oxides (tungstic acids, $WO_3{\cdot}H_2O$ and $WO_3{\cdot}2\ H_2O$), enabled by the highly acidic electrolyte pH [29,55,64]. This precipitation took place following a polycondensation mechanism, in such a way that a nanostructured layer was formed [29,55]. The formation of this nanostructured layer partially blocked the interfacial flow of electrons, resulting in a decrease in current density, as observed in the third and last region of the curves. It is clearly seen that the higher the % of M. azedarach leaves extract in the electrolyte, the later current density began to decrease in the third stage. In fact, for the sample anodized with 10% of extract, current density dropped very slowly. This result can be attributed to the tendency of polyphenolic molecules to maintain tungsten species in

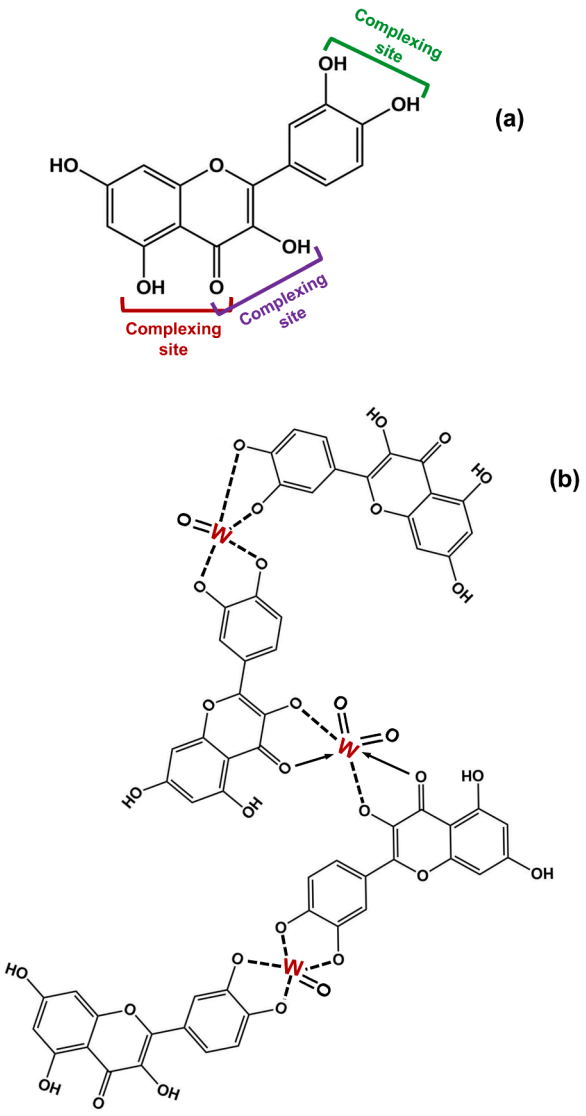

Fig. 2. (a) Molecule of quercetin, a typical polyphenolic compound (flavonoid), with the three possible metal-complexation sites labelled; (b) example of tungsten complexation by quercetin molecules.

solution through strong complexing interactions, therefore delaying W-polycondensates precipitation in the form of tungstic acids.

3.2. FESEM, HRTEM and XRD

To analyze the influence of M. azedarach leaves extract on the morphology of the formed nanostructures, FESEM images were taken at different magnifications. In Fig. 3, images obtained at 10,000 magnifications are shown for the blank sample and for samples anodized with various extract percentages (1%, 3%, 5%, 7% and 10%). Clear differences can be discerned between the morphology of the blank sample (Fig. 3a) and that of the samples anodized with M. azedarach leaves extract (Fig. 3b–f). For the blank sample, big nanoplates were formed on a thin layer of approximately spherical nanoparticles (see Fig. 3a and Figure S1a in the Supporting Information). When M. azedarach leaves extract was present in the anodization electrolyte, morphology of nanostructures noticeably changed. Nanoplates disappeared and small spherical nanoparticles or short nanorods formed homogeneous and very porous or spongy layers (Fig. 3b and Figure S1b in the Supporting Information). The size of these short nanorods slightly decreased with increasing % of extract, since polyphenolic species concentration also increased, thus enhancing the complexing capacity of the electrolyte [38,50]. However, for the sample anodized in the presence of 10% extract (Fig. 3f), these nanorods started to deform (flatten), maybe due to the high concentration of complexing agents in the solution.

Fig. 4 represents the mean thickness of the nanostructured layers formed on the different samples. It can be seen that thickness increased with increasing M. azedarach extract percentage until reaching a maximum for the sample anodized with 5% extract, and then decreased. In this case, two opposing phenomena are responsible for this result. As the percentage of M. azedarach leaves extract raised, tungsten dissolution was favored and the amount of complex soluble species near the electrode surface was higher. Hence, more matter precipitated and the formed nanostructured layer was thicker. However, an increase in the extract percentage also enhanced the capacity of polyphenolic molecules to keep tungsten species in solution, in the form of complex compounds. Therefore, the first phenomenon (higher dissolution and higher precipitation) prevailed over the second one (stabilization of complex soluble species) until extract percentages of 5% or lower were reached. For higher percentages, the second phenomenon was the predominant one. Anyway, observing images in Fig. 3 and thickness data in Fig. 4, it can be concluded that nanostructures fabricated with an extract percentage of 5% provided the highest specific surface to the electrolyte, since its morphology was very porous/spongy and its thickness was the largest.

XRD analysis was carried out to study the possible influence of the electrolyte composition on the crystallinity of WO_3 nanostructures. Fig. 5 displays the XRD patterns for the blank sample and for samples anodized in the presence of 2%, 5% and 10% M. azedarach extract. All samples provided the same pattern with similar peaks, corresponding to monoclinic WO_3 [27,69–72]. Scherrer's equation has been used to obtain the crystallite size (D) of the different samples, knowing that the shape factor k is 0.9, the X-ray wavelength λ is 0.15406 nm, the full-width at half maximum intensity is obtained from each peak (in rad) and θ is the Bragg angle (also in rad) [73]:

$$D = \frac{k \bullet \lambda}{w \bullet \cos\theta} \quad (1)$$

The main peak at 2θ of ca. 23º has been used, which is a triplet actually, corresponding with the (002), (020) and (200) crystalline planes of the monoclinic WO_3 [27,69–72]. The average crystallite sizes are the following: 44.84 nm for the blank sample, 42.68 nm for the 2% sample, 40.70 nm for the 5% sample and 44.66 nm for the 10% sample. The lowest crystallite size is observed for the sample anodized with 5% M. azedarach extract, while the highest size corresponds to the blank sample together with the sample anodized with 10% extract. This result is consistent with the dimensions of nanorods visually analyzed with FESEM images (Fig. 3). Indeed, it has been observed that as the % of leaf extract increased in the anodization electrolyte (until 5% was reached), smaller nanorods were obtained, since the complexing ability of polyphenols and other organic molecules in the extract contributed to a controlled precipitation process and, therefore, to the reduction of the nanorods size. At higher leaf extract percentage (10%), nanorods started deforming due probably to chemical etching, and nanorods were distorted. Therefore, it is reasonable that crystallite sizes followed the same tendency, reaching a minimum for the sample anodized in the presence of 5% leaf extract.

The FESEM study has allowed knowing the morphology of the formed WO_3 nanostructures. Further studies with transmission electron microscopy can provide additional information (phases formed as well as the morphology using higher magnifications by HR-TEM). Conversely to FESEM, the TEM study has been undertaken analyzing the material obtained after scratching the tungsten oxide layer. Fig. 6 shows the TEM images of the samples synthesized with and without extract. The reference sample not anodized with extract (blank sample), mainly consisted of large entities (80–800 nm) with no or low porosity which seemed not to be formed by the aggregation of small units. Moreover, smaller

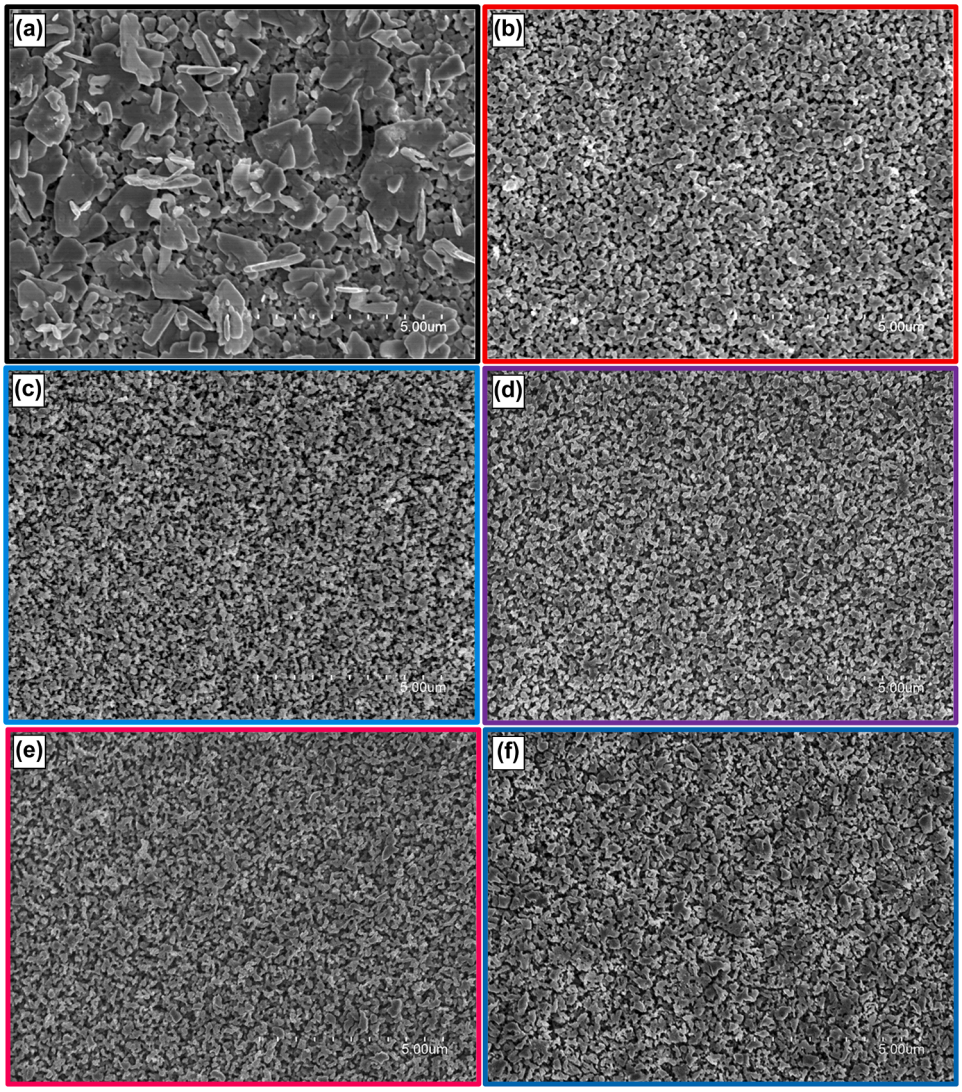

Fig. 3. FESEM images obtained at 10,000 magnifications for the blank sample (a) and for samples anodized with various extract percentages: (b) 1%, (c) 3%, (d) 5%, (e) 7% and (f) 10%.

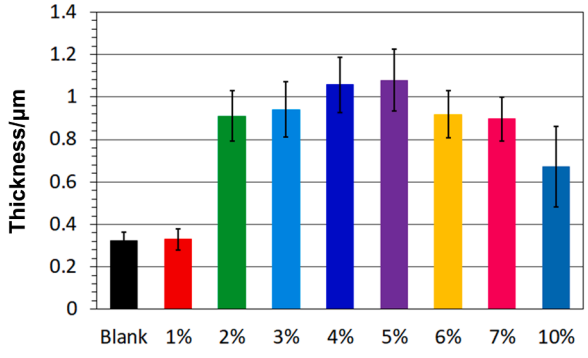

Fig. 4. Mean thickness of the nanostructured layers formed on the different samples.

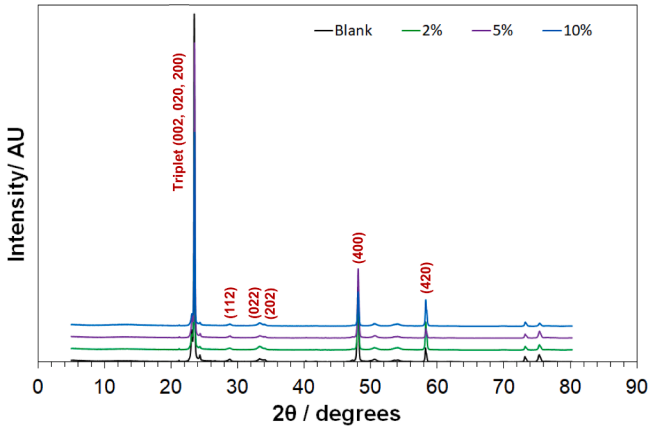

Fig. 5. XRD patterns for the blank sample and for samples anodized in the presence of 2%, 5% and 10% M. azedarach extract.

entities of different sizes could also be observed. However, the use of the extract during anodization substantially changed the morphology. In the case of the sample synthesized with 3% extract, large aggregations of nanoparticles were mainly observed. Many of these aggregations were in the order of micrometers and were formed of particles with typical lengths of 30–120 nm. The samples prepared with higher concentration of extract (5 and 10%) were also formed by aggregations of nanoparticles. However, these aggregations were, in average, smaller than those for the 3% sample. Interestingly, differences in the size of the

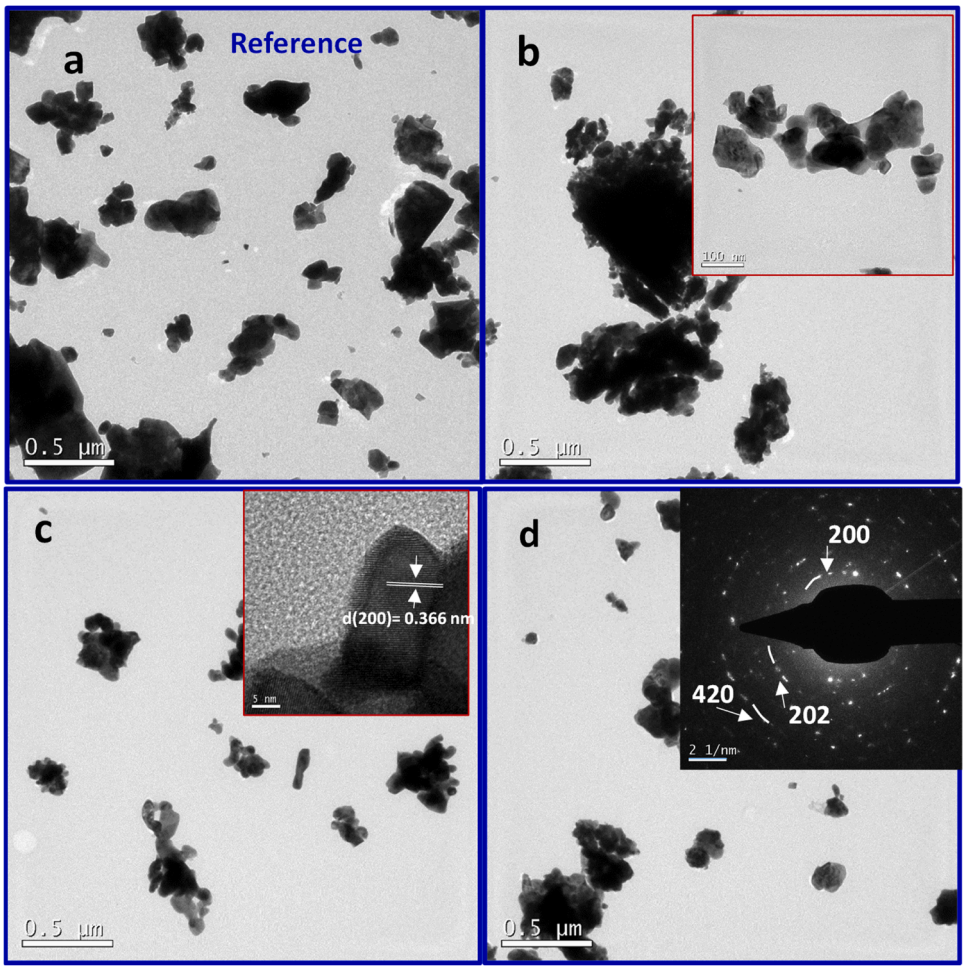

Fig. 6. Transmission electron microscopy (TEM) images of the samples synthesized without (a) or with extracts (b to d) during the anodization: 3% (b), 5% (c), 10% (d). Additional TEM image of the 3% sample (inset, b), a High Resolution TEM image of 5% sample (inset, c) and the corresponding SAED patterns of WOx of 10% sample (inset, d) are also included.

nanoparticles were detected between the 5 and 10% samples, in agreement with that observed by FESEM. Then, the nanoparticles of 5% sample were smaller (mainly ranging from 20 to 60 nm) than those of the 10% sample (mainly ranging from 20 to 90 nm). It is worth noting that certain porosity could be observed in the samples treated with extract.

The analysis of the interplanar distances of all the samples by high Resolution TEM as well as the SAED study confirms, in agreement with that observed by XRD, that the samples were formed of monoclinic WO_3 phase. No W has been detected, confirming that the scratching of the sample has been highly superficial. Interplanar distances at 1.58 Å, 2.63 Å and 3.65 Å associated with the Bragg lines of (420), (202) and (200) corresponding to monoclinic tungsten oxide (JCPDS: 43–1035) have been clearly observed although the level of crystallinity is not elevated (Fig. 6d).

3.3. (Photo)electrochemical characterization: impedance measurements and photocurrent density vs potential curves

Electrochemical Impedance Spectroscopy (EIS) measurements were performed to investigate electrochemical processes at the nanostructures/electrolyte interface. Nyquist and Bode-phase plots are presented in Fig. 7. In Nyquist plots (Fig. 7a), two incomplete semicircles were obtained, one at medium frequencies (see enlarged plot) and another one at low frequencies. The smaller first semicircle can be associated with the interfacial charge transfer of the nanostructures, while the second semicircle, much larger, accounts for the electrochemical response of the remaining compact WO_3 film at the bottom of the nanostructured layer [74]. Therefore, the first (smaller) semicircle is the interesting one, since it is directly related to the interfacial specific area of the nanostructures. Observing the enlarged plot in Fig. 7a (right), it is clear that the sample with the lowest semicircle was the one anodized with 5% extract, while the blank sample yielded the highest impedance values.

Bode-phase plots (Fig. 7b) show two visible bands, directly related to the two semicircles (at medium and low frequencies) observed above in Nyquist plots. Consequently, in order to quantitatively discuss EIS results, an equivalent electrical circuit with two R-CPE time constants hierarchically associated (see inset in Fig. 7b) has been used. R_S represents electrolyte resistance, while R-CPE elements account for the resistance and capacitance of the nanostructured electrical double layer (1) and for the compact WO_3 film underneath the nanostructured layer (2) [29,74]. It is worth remarking that in this circuit, Constant Phase Elements (CPE) have been used instead of pure capacitances to consider the non-ideal behavior of real capacitors.

Resistance values for all the samples are presented in Table 1. In all cases, chi-square values were of the order of 10^{-3} or even 10^{-4}, indicating the good fitting of the circuit to the experimental data. Electrolyte resistances (R_S) were similar for all the samples, since the electrolyte and the experimental set-up was always the same. The highest value for the resistance of the nanostructure (interfacial charge-transfer processes) (R_1) was for the blank sample, decreasing with growing extract

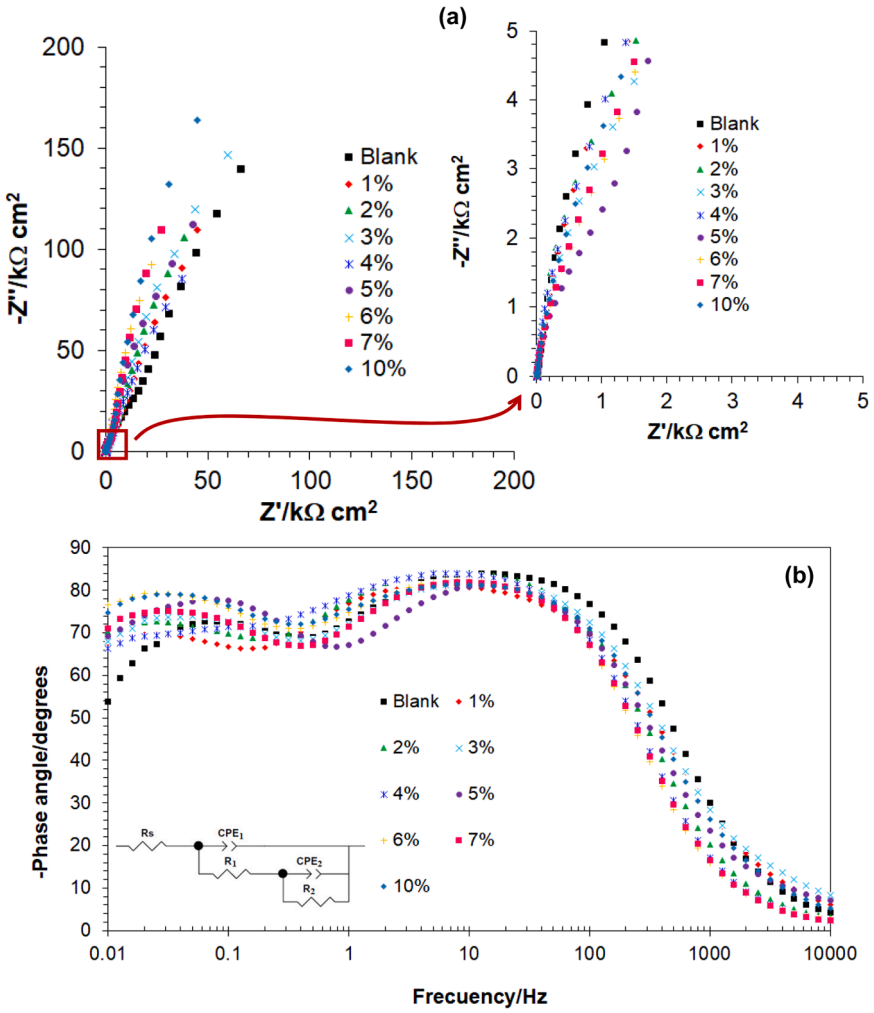

Fig. 7. Nyquist (a) and Bode-phase (b) plots of the WO_3 nanostructures fabricated without (blank) and with different extract percentages.

Table 1
Resistance values calculated from EIS data for all the WO_3 nanostructures.

Sample	R_S (Ω·cm²)	R_1 (kΩ·cm²)	R_2 (GΩ·cm²)	X^2 (×10⁻³)
Blank	10.1	70.8	5.7	2.4
1%	10.2	43.0	5.5	0.5
2%	10.0	16.8	6.5	0.6
3%	10.2	14.4	5.9	2.9
4%	9.6	12.8	6.9	0.3
5%	10.0	5.4	6.3	2.8
6%	9.6	8.4	5.7	1.0
7%	9.6	11.3	6.2	0.5
10%	9.9	23.9	8.6	2.7

percentage until reaching a minimum value for the 5% extract sample, and then began increasing again. This result can be ascribed to an increase in specific surface area for nanostructures anodized in the presence of M. azedarach leaves extract, reaching a maximum specific surface value with 5% extract. The previous explanation is consistent with the morphology of the samples (Fig. 3) and with the thickness of the nanostructured layers (Fig. 4). Finally, resistance values of the compact WO_3 film formed at the bottom of the samples (R_2) were much higher than R_1 and of the same order of magnitude, regardless of the sample.

Mott-Schottky analysis was also performed to study the semiconducting behavior of the WO_3 nanostructures, as well as to evaluate their defectiveness, in order to use these samples in photoelectrocatalytic applications. Fig. 8 shows the Mott-Schottky plots of the

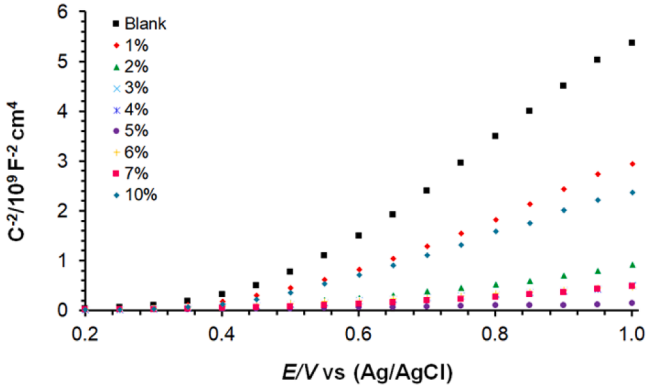

Fig. 8. Mott-Schottky plots of the WO_3 nanostructures fabricated without (blank) and with different extract percentages.

different nanostructures. It can be observed that a clear linear region with positive slope was obtained for all the samples, indicating an *n*-type semiconducting behavior. According to Mot-Schottky equation:

$$\frac{1}{C^2} = \frac{1}{C_H^2} + \frac{2}{\varepsilon_r \varepsilon_0 e N_D}\left(E - E_{FB} - \frac{k_B T}{e}\right) \quad (2)$$

the value of density of defects or donor species N_D (in cm^{-3}), which are oxygen vacancies in the case of WO_3, could be determined from the

different slopes. The other parameters in Mott-Schottky equation are: C_H (capacitance of the Helmholtz layer), ε_r (relative permittivity or dielectric constant of WO_3 nanostructures (50) [75,76]), ε_0 (vacuum permittivity, $8.85{\cdot}10^{-14}$ F cm^{-1}), e (elementary charge, $1.60{\cdot}10^{-19}$ C), E_{FB} (flat-band potential, in V), k_B (Boltzmann constant, $1.38{\cdot}10^{-23}$ J K^{-1}) and T (absolute temperature, in K).

From Fig. 8, it is seen that the positive slope of the linear region decreased with increasing extract percentage in the anodization electrolyte, reaching again a minimum value for the sample fabricated with 5% extract. For higher percentages, the slope began increasing again. Oxygen vacancies density (N_D) are presented in Table 2. The highest N_D value was reached by the 5% extract sample, while the lowest value corresponded to the blank sample. These results complement those previously obtained from EIS measurements, since high donor densities generally correlate with low interfacial charge-transfer resistances and vice versa. Hence, the highest value of N_D for the sample synthesized with the 5% extract is also a result of its highest specific surface area, resulting in low resistances, therefore favoring charge transfer processes and making this nanostructure a very good candidate for electrochemical and photoelectrochemical applications.

Photoelectrochemical properties of the WO_3 nanostructures were also examined by means of linear sweep voltammetries recorded while applying pulses of dark and simulated solar light conditions. This kind of plot permits determine the photoelectrochemical response of the samples (by measuring their photocurrent densities) and, at the same time, assess their stability towards photodegradation (through their dark current densities). Fig. 9a shows the different potential-(photo)current density curves for the WO_3 nanostructures. Upon illumination with simulated solar light, high photocurrent densities, i_{ph} (pulses), were obtained for all the samples, whereas very low (of the order of several μA cm^{-2}) dark current densities were obtained without illumination. Photocurrent densities also increased with applied potential. The highest i_{ph} values were recorded for the 5% extract sample, which is consistent with previous results. Thus, the high specific surface area of this sample resulted in more photon hitting sites and, consequently, in a higher number of photogenerated electron-hole pairs. In Fig. 9b, this tendency of photocurrent densities is more visibly shown at two different potentials: 0.72 V and 1.05 V. It is observed that for both potentials, the maximum i_{ph} value was reached for the sample labelled as 5%.

DR-UV-Vis. spectra of WO_3 nanostructures synthesized by the anodization of tungsten in the presence of extracts are shown in Figure S2. In all cases, the general shape of the spectra mainly consists of one main absorption band in the UV region until ca. 450 nm, which corresponds to a typical inter-band transition of bulk WO_3, consistent with the monoclinic structure [77]. The band gap energies of tungsten oxide nanostructures were also determined through the Tauc plot. Band gaps around 2.78 eV were observed for all the samples regardless of the use of extracts during the synthesis procedure. These values are in the usual energy range reported for monoclinic WO_3 nanostructures (from 2.5 eV to 3.00 eV) [78].

Table 2
Donor density values (N_D) for all the WO_3 nanostructures.

Sample	N_D (cm^{-3}) × 10^{20}
Blank	2.8
1%	5.1
2%	18.0
3%	41.2
4%	41.7
5%	103.8
6%	37.4
7%	34.6
10%	6.3

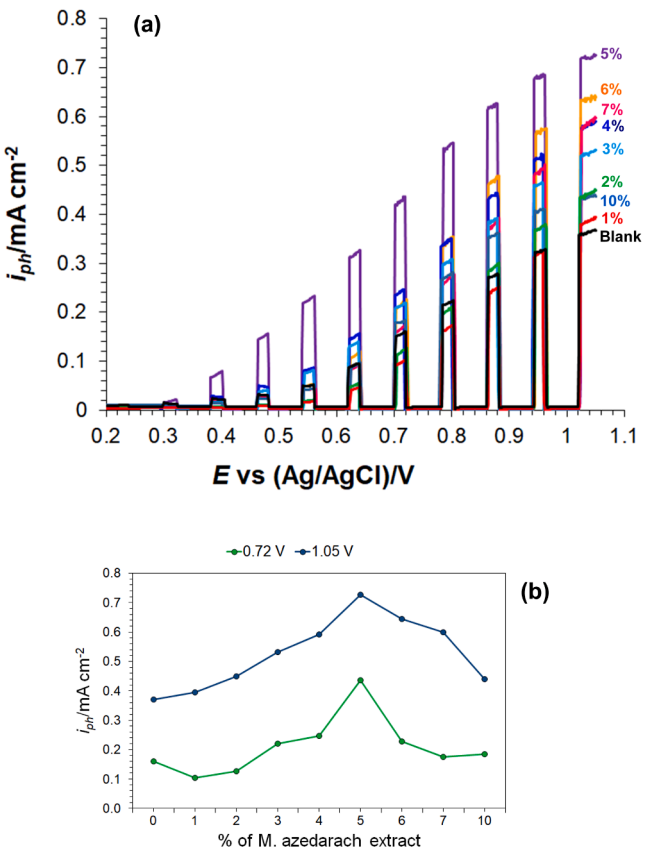

Fig. 9. (a) Potential-(photo)current density curves for the WO_3 nanostructures. (b) Variation of the maximum photocurrent density value with extract percentage, recorded at two applied potentials: 0.72 V and 1.05 V.

3.4. Evaluation of WO_3 nanostructures as Li-ion battery anodes

Fig. 10a displays the galvanostatic charge/discharge curves for the WO_3 nanostructure fabricated with the 5% M. azedarach extract, since it has been the nanostructure with the best electrochemical performance. In this figure, variation of potential vs specific capacity is shown for the WO_3 (anode)/Li (cathode) battery, at different cycles and at a rate of 0,1 C. Hence, anode charge curves correspond with the charging of the WO_3 anode, that is, with the insertion of Li^+ within the oxide lattice, while anode discharge curves refer to the Li^+ extraction process from the Li_xWO_3 structure.

The first charge and discharge cycles provided a specific capacity of 933.5 mAh/g and 365.6 mAh/g, respectively, resulting in a reversible coulombic efficiency (i.e. the ratio between extraction and insertion capacities) of only 39.2%. This low efficiency can be explained considering the first charge (Li^+ insertion) curve, whose specific capacity was much higher than for the rest of cycles. In the charge curve of cycle 1 there are some unique features which were not repeated in subsequent cycles and which, therefore, are related to different irreversible processes. First, the initial potential drop was followed by a potential plateau at ~1.7 V, which can be associated with some irreversible phase transformation and/or with the formation of a solid electrolyte interface (SEI) on the WO_3 surface [79,80]. A second, and shorter, potential plateau appeared at ~0.7–0.8 V, which has also been usually ascribed to electrolyte decompositions in the low potential region and irreversible formation of a SEI [79,81] or to some permanent lithium insertion within the WO_3 lattice caused by irreversible phase transformations [79,82]. Some authors relate the plateau around 0.7–0.8 V to the electrochemical reduction of W^{6+} to metallic W and the formation of amorphous Li_2O [81,83], according to the next conversion reaction:

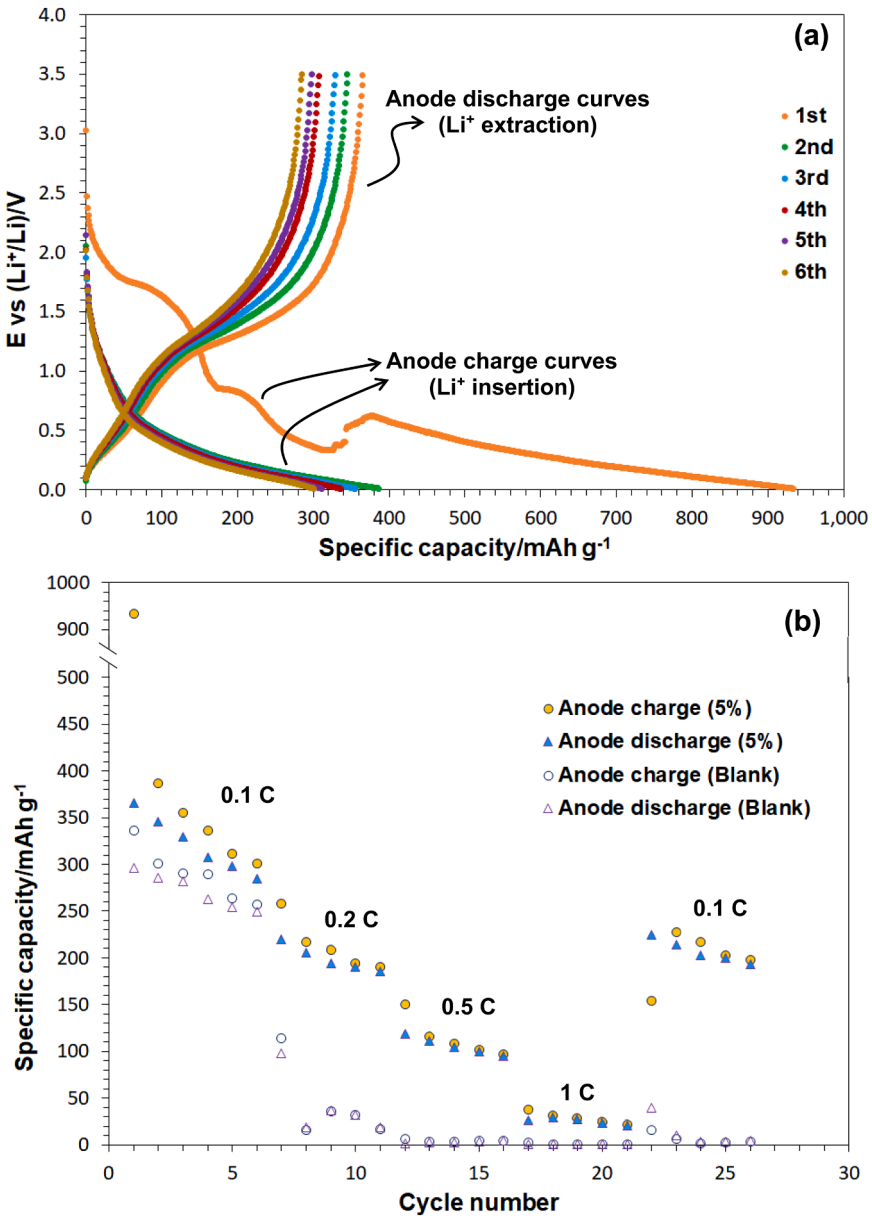

Fig. 10. (a) Galvanostatic charge/discharge curves for the WO_3 nanostructure fabricated with the 5% M. azedarach extract, with a cycling rate of 0.1 C. (b) Specific capacity vs number of cycles of the WO_3 sample fabricated in the presence of 5% M. azedarach extract (results for the blank Fig. 10. (a) Galvanostatic charge/discharge curves for the WO_3 nanostructure fabricated with the 5% M. azedarach extract, with a cycling rate of 0.1 C. (b) Specific capacity vs number of cycles of the WO_3 sample fabricated in the presence of 5% M. azedarach extract (results for the blank sample are also shown for comparison purposes).

$$Li_XWO_3 + (6\text{-}x)\ Li \rightarrow W + 3\ Li_2O \quad (3)$$

However, the previous process has also been linked to the plateau appearing at ~0.3–0.4 V (and, in the present case, the small potential increase, as well) [80,84]. This process has been identified as responsible for certain degree of changes (destruction or deformation) of the WO_3 crystal structure [80,81,85], which would be another irreversible process with influence on the decrease of coulombic efficiency. Finally, the large sloping region of the first discharge curve (until 0 V) has been explained by reaction processes between the WO_3 and the electrolyte [84].

Regardless of the particular origin of all the potential plateaus and low-voltage sloping regions, it is clear that all these features in the first charge curve are caused by interfacial irreversible processes. Therefore, these issues did not appear in successive charge curves, whose features were simpler. The potential drop from 3.5 V to approximately 0.7 V is normally attributed to the reaction [82,84]:

$$WO_3 + x\ Li^+ + x\ e^- \rightarrow Li_XWO_3 \quad (4)$$

This process was followed, from 0.7 V to 0 V, by a softer potential decrease, corresponding to the conversion reaction (3), explained before. Therefore, the global electrochemical process between Li ions and WO_3 nanostructures can be summarized as [84]:

$$WO_3 + 6\ Li^+ + 6\ e^- \rightarrow W + 3\ Li_2O \quad (5)$$

Concerning discharge curves (Li^+ extraction from the anode), differences between cycles were much smaller than for charge curves. Potential started to increase constantly from 0 V to approximately 1.3 V due to lithium extraction process. The tendency of this increase changed between 1.3 and 1.5 V with a pseudo-plateau, which may be related to the oxidation reaction of W^0 to W^{6+} [81,83]. After that, Li^+ extraction continued until a potential of 3.5 V was reached. Both processes (Li^+

extraction and W oxidation) took place reversibly, since all discharge curves showed the same features.

Fig. 10b shows the cycling performance of the WO_3 sample fabricated in the presence of 5% M. azedarach extract, by plotting the specific capacity vs the number of cycles at the different cycling rates. Results for a blank sample (i.e, synthesized without M. azedarach extract) are also shown to compare. It can be seen that the biosynthesized WO_3 nanostructure provided higher specific capacities, regardless of the cycling rate. Besides, this sample significantly recovered its specific capacity after fast charge/discharge cycles (0.1 C cycling at the end of tests), while blank sample lost a great amount of its initial specific capacity. This result indicates that big nanoplates and nanoparticles (blank sample) were unstable under different charge-discharge rates compared with short nanorods forming spongy layers (biosynthesized sample). For both samples, capacities decreased with increasing cycling rates, which is normal, due to internal resistances, difficulty for Li^+ ions to transport at these high rates, etc. It can also be observed that reversible coulombic efficiencies for the M. azedarach-mediated WO_3 nanostructure was very high, apart from the first charge/discharge cycle at 0.1 C, where an important irreversibility was observed, as it has been commented above. Differences observed between both samples can be explained by a significantly higher surface area of the biosynthesized WO_3 nanorods compared with that of WO_3 nanoplates of the blank sample. These results, therefore, confirm the better performance of bio-mediated WO_3 nanostructure as negative electrodes in Li-ion batteries. However, several issues must be improved in the future, such as higher reversible coulombic efficiency and enhanced specific capacities, especially at high cycling rates.

4. Conclusions

Monoclinic WO_3 nanostructures have been fabricated by electrochemical anodization in the presence of different amounts of *Melia azedarach* leaves extract. The formation mechanism was based on a dissolution-precipitation process, and in all the cases, short nanorods were formed. However, at extract percentages between 4% and 6%, these nanorods were smaller, thus exposing higher specific surfaces, which was confirmed by HR-TEM analyses.

Resistance of WO_3 nanorods to charge transfer processes decreased with increasing the percentage of leaves extract until reaching a minimum for 5%. Density of defects (oxygen vacancies for *n*-type semiconductor WO_3) increased with increasing the percentage of leaves extract until reaching a maximum for 5%. This behavior can be ascribed to the substantial increase in the WO_3 nanorods specific surface for extract percentages around 5%. The high specific surface area of these nanorods was fundamental for their excellent behavior as photoelectrocatalysts, enhancing the interaction with photons and promoted the formation of photogenerated electron-hole pairs. Moreover, nanorods anodized in the presence of 5% leaves extract displayed high specific capacities as Li-ion battery anodes and good cyclability compared with the blank sample (anodized without biogenic compounds), although the formation of a solid electrolyte interface (SEI) resulted in an irreversible loss of capacity between the first and subsequent cycles. This phenomenon should be solved in the future to improve the performance of these nanostructures as electrodes in rechargeable Li-ion devices.

All results obtained in this work confirm that anodization of tungsten in the presence of biogenic molecules from M.azedarach leaves extract resulted in high aspect ratio WO_3 nanorods with great photoelectrocatalytic performance and promising behavior as Li-ion anodes. Therefore, the new methodology for the fabrication of nanostructures presented in this work, which combines the simplicity and versatility of electrochemical anodization with all the advantageous green aspects of using biogenic electrolytes, could represent and important improvement not only in the nanomaterials field, but in the energetic one.

CRediT authorship contribution statement

Benjamin Solsona: Writing – original draft, Validation, Supervision, Methodology, Funding acquisition, Formal analysis. **Ramón M. Fernández-Domene:** Writing – original draft, Supervision, Methodology, Investigation, Funding acquisition, Formal analysis, Data curation, Conceptualization. **Encarna Blasco-Tamarit:** Validation, Resources. **Maria Erans:** Validation, Resources. **Rita Sanchez-Tovar:** Validation, Supervision, Resources, Funding acquisition, Formal analysis.

Declaration of Competing Interest

The authors declare that they have no known competing financial interests or personal relationships that could have appeared to influence the work reported in this paper.

Data Availability

Data will be made available on request.

Acknowledgements

M. Erans is grateful for Grant RYC2021–031428-I funded by MCIN/AEI/ 10.13039/501100011033 and by European Union NextGenerationEU/PRTR. Authors would also like to acknowledge the Generalitat Valenciana for CIAICO/2021/094, CIGRIS/2022/198 and CIGE/2022/166. Authors also would like to acknowledge the Ministerio de Ciencia e Innovación-Agencia Estatal de Investigación through the projects PID2021–126235OB-C33 MCIN/AEI/10.13039/501100011033/FEDER Una manera de hacer Europa, UE and TED2021–129555B-I00/ AEI/ 10.13039/ 501100011033/Unión Europea NextGenerationEU/PRTR. Thanks to SCSIE-UV for assistance in characterization of materials.

Appendix A. Supporting information

Supplementary data associated with this article can be found in the online version at doi:10.1016/j.jallcom.2024.174845.

References

[1] BP, BP Statistical Review of World Energy 2022,(71st edition), ⟨Https://Www.Bp.Com/Content/Dam/Bp/Business-Sites/En/Global/Corporate/Pdfs/Energy-Economics/Statistical-Review/Bp-Stats-Review-2022-Full-Report.Pdf⟩. (2022) 1–60. ⟨https://www.bp.com/content/dam/bp/business-sites/en/global/corporate/pdfs/energy-economics/statistical-review/bp-stats-review-2022-full-report.pdf⟩.

[2] M.A. Rosen, S. Koohi-Fayegh, The prospects for hydrogen as an energy carrier: an overview of hydrogen energy and hydrogen energy systems, Energy Ecol. Environ. 1 (2016) 10–29, https://doi.org/10.1007/s40974-016-0005-z.

[3] Z. Abdin, A. Zafaranloo, A. Rafiee, W. Mérida, W. Lipiński, K.R. Khalilpour, Hydrogen as an energy vector, Renew. Sustain. Energy Rev. 120 (2020) 109620, https://doi.org/10.1016/j.rser.2019.109620.

[4] S.K. Dewangan, M. Mohan, V. Kumar, A. Sharma, B. Ahn, A comprehensive review of the prospects for future hydrogen storage in materials-application and outstanding issues, Int. J. Energy Res. 46 (2022) 16150–16177, https://doi.org/10.1002/er.8322.

[5] M. Hirscher, V.A. Yartys, M. Baricco, J. Bellosta von Colbe, D. Blanchard, R. C. Bowman, D.P. Broom, C.E. Buckley, F. Chang, P. Chen, Y.W. Cho, J.-C. Crivello, F. Cuevas, W.I.F. David, P.E. de Jongh, R.V. Denys, M. Dornheim, M. Felderhoff, Y. Filinchuk, G.E. Froudakis, D.M. Grant, E.M. Gray, B.C. Hauback, T. He, T. D. Humphries, T.R. Jensen, S. Kim, Y. Kojima, M. Latroche, H.-W. Li, M. V. Lototskyy, J.W. Makepeace, K.T. Møller, L. Naheed, P. Ngene, D. Noréus, M. M. Nygård, S. Orimo, M. Paskevicius, L. Pasquini, D.B. Ravnsbæk, M. Veronica Sofianos, T.J. Udovic, T. Vegge, G.S. Walker, C.J. Webb, C. Weidenthaler, C. Zlotea, Materials for hydrogen-based energy storage – past, recent progress and future outlook, J. Alloys Compd. 827 (2020) 153548, https://doi.org/10.1016/j.jallcom.2019.153548.

[6] P. Chatterjee, M.S.K. Ambati, A.K. Chakraborty, S. Chakrabortty, S. Biring, S. Ramakrishna, T.K.S. Wong, A. Kumar, R. Lawaniya, G.K. Dalapati, Photovoltaic/photo-electrocatalysis integration for green hydrogen: a review, Energy Convers. Manag. 261 (2022) 115648, https://doi.org/10.1016/j.enconman.2022.115648.

[7] Z.J. Baum, L.L. Diaz, T. Konovalova, Q.A. Zhou, Materials research directions toward a green hydrogen economy: a review, ACS Omega 7 (2022) 32908–32935, https://doi.org/10.1021/acsomega.2c03996.

[8] R. Abe, Recent progress on photocatalytic and photoelectrochemical water splitting under visible light irradiation, J. Photochem. Photobiol. C Photochem. Rev. 11 (2010) 179–209, https://doi.org/10.1016/j.jphotochemrev.2011.02.003.
[9] A. Eftekhari, V.J. Babu, S. Ramakrishna, Photoelectrode nanomaterials for photoelectrochemical water splitting, Int. J. Hydrog. Energy 42 (2017) 11078–11109, https://doi.org/10.1016/j.ijhydene.2017.03.029.
[10] M.B. Costa, M.A. de Araújo, M.V. d L. Tinoco, J.F. d Brito, L.H. Mascaro, Current trending and beyond for solar-driven water splitting reaction on WO3 photoanodes, J. Energy Chem. 73 (2022) 88–113, https://doi.org/10.1016/j.jechem.2022.06.003.
[11] L. Clarizia, M.N. Nadagouda, D.D. Dionysiou, Recent advances and challenges of photoelectrochemical cells for hydrogen production, Curr. Opin. Green. Sustain. Chem. 41 (2023) 100825, https://doi.org/10.1016/j.cogsc.2023.100825.
[12] S. Goriparti, E. Miele, F. De Angelis, E. Di Fabrizio, R. Proietti Zaccaria, C. Capiglia, Review on recent progress of nanostructured anode materials for Li-ion batteries, J. Power Sources 257 (2014) 421–443, https://doi.org/10.1016/j.jpowsour.2013.11.103.
[13] P. Roy, S.K. Srivastava, Nanostructured anode materials for lithium ion batteries, J. Mater. Chem. A. 3 (2015) 2454–2484, https://doi.org/10.1039/c4ta04980b.
[14] M.S. Balogun, W. Qiu, Y. Luo, H. Meng, W. Mai, A. Onasanya, T.K. Olaniyi, Y. Tong, A review of the development of full cell lithium-ion batteries: the impact of nanostructured anode materials, Nano Res 9 (2016) 2823–2851, https://doi.org/10.1007/s12274-016-1171-1.
[15] W. Qi, J.G. Shapter, Q. Wu, T. Yin, G. Gao, D. Cui, Nanostructured anode materials for lithium-ion batteries: principle, recent progress and future perspectives, J. Mater. Chem. A. 5 (2017) 19521–19540, https://doi.org/10.1039/c7ta05283a.
[16] S. Sanati, Z. Rezvani, B. Habibi, The NiGa-LDH@NiWO4 nanocomposite as an electrode material for pseudocapacitors, N. J. Chem. 42 (2018) 18426–18436, https://doi.org/10.1039/c8nj04402c.
[17] L.P. Yu, X.H. Zhou, L. Lu, X.L. Wu, F.J. Wang, Recent developments of nanomaterials and nanostructures for high-rate lithium ion batteries, ChemSusChem 13 (2020) 5361–5407, https://doi.org/10.1002/cssc.202001562.
[18] Y. Pan, S. Sanati, R. Abazari, V.N. Noveiri, J. Gao, A.M. Kirillov, Pillared-MOF@NiV-LDH composite as a remarkable electrocatalyst for water oxidation, Inorg. Chem. 61 (2022) 20913–20922, https://doi.org/10.1021/acs.inorgchem.2c03327.
[19] H. Xu, H. Li, X. Wang, The anode materials for lithium-ion and sodium-ion batteries based on conversion reactions: a review, ChemElectroChem 10 (2023) e202201151, https://doi.org/10.1002/celc.202201151.
[20] J. Du, Q. Li, J. Chai, L. Jiang, Q. Zhang, N. Han, W. Zhang, B. Tang, Review of metal oxides as anode materials for lithium-ion batteries, Dalt. Trans. 51 (2022) 9584–9590, https://doi.org/10.1039/d2dt01415g.
[21] A. Eftekhari, Low voltage anode materials for lithium-ion batteries, Energy Storage Mater. 7 (2017) 157–180, https://doi.org/10.1016/j.ensm.2017.01.009.
[22] T. Kim, W. Song, D.Y. Son, L.K. Ono, Y. Qi, Lithium-ion batteries: outlook on present, future, and hybridized technologies, J. Mater. Chem. A 7 (2019) 2942–2964, https://doi.org/10.1039/C8TA10513H.
[23] J. Li, J. Fleetwood, W.B. Hawley, W. Kays, From materials to cell: state-of-the-art and prospective technologies for lithium-ion battery electrode processing, Chem. Rev. 122 (2022) 903–956, https://doi.org/10.1021/acs.chemrev.1c00565.
[24] P.U. Nzereogu, A.D. Omah, F.I. Ezema, E.I. Iwuoha, A.C. Nwanya, Anode materials for lithium-ion batteries: a review, Appl. Surf. Sci. Adv. 9 (2022) 100233, https://doi.org/10.1016/j.apsadv.2022.100233.
[25] H. Zheng, J.Z. Ou, M.S. Strano, R.B. Kaner, A. Mitchell, K. Kalantar-Zadeh, Nanostructured tungsten oxide - properties, synthesis, and applications, Adv. Funct. Mater. 21 (2011) 2175–2196, https://doi.org/10.1002/adfm.201002477.
[26] C.A. Bignozzi, S. Caramori, V. Cristino, R. Argazzi, L. Meda, A. Tacca, Nanostructured photoelectrodes based on WO3: applications to photooxidation of aqueous electrolytes, Chem. Soc. Rev. 42 (2013) 2228–2246, https://doi.org/10.1039/c2cs35373c.
[27] R. Abazari, S. Sanati, Room temperature synthesis of tungsten (VI) tri-oxide nanoparticles with one-pot multi-component reaction in emulsion nanoreactors stabilized by aerosol-OT, Mater. Lett. 107 (2013) 329–332, https://doi.org/10.1016/j.matlet.2013.06.045.
[28] S.S. Kalanur, L.T. Duy, H. Seo, Recent progress in photoelectrochemical water splitting activity of WO3 photoanodes, Top. Catal. 61 (2018) 1043–1076, https://doi.org/10.1007/s11244-018-0950-1.
[29] R.M. Fernández-Domene, G. Roselló-Márquez, R. Sánchez-Tovar, M. Cifre-Herrando, J. García-Antón, Synthesis of WO3 nanorods through anodization in the presence of citric acid: formation mechanism, properties and photoelectrocatalytic performance, Surf. Coat. Technol. 422 (2021) 127489, https://doi.org/10.1016/j.surfcoat.2021.127489.
[30] M. Shah, D. Fawcett, S. Sharma, S.K. Tripathy, G.E.J. Poinern, Green synthesis of metallic nanoparticles via biological entities, Mater. (Basel) 8 (2015) 7278–7308, https://doi.org/10.3390/ma8115377.
[31] S. Ahmed, Annu, S.A. Chaudhry, S. Ikram, A review on biogenic synthesis of ZnO nanoparticles using plant extracts and microbes: a prospect towards green chemistry, J. Photochem. Photobiol. B Biol. 166 (2017) 272–284, https://doi.org/10.1016/j.jphotobiol.2016.12.011.
[32] N.A.I. Md Ishak, S.K. Kamarudin, S.N. Timmiati, Green synthesis of metal and metal oxide nanoparticles via plant extracts: an overview, Mater. Res. Express 6 (2019) 112004, https://doi.org/10.1088/2053-1591/ab4458.
[33] R.M.C.R. Ramos, M.D. Regulacio, Controllable synthesis of bimetallic nanostructures using biogenic reagents: a green perspective, ACS Omega 6 (2021) 7212–7228, https://doi.org/10.1021/acsomega.1c00692.
[34] V. Batra, I. Kaur, D. Pathania, Sonu, V. Chaudhary, Efficient dye degradation strategies using green synthesized ZnO-based nanoplatforms: a review, Appl. Surf. Sci. Adv. 11 (2022) 100314, https://doi.org/10.1016/j.apsadv.2022.100314.
[35] T.R. Lakshmeesha, M. Murali, M.A. Ansari, A.C. Udayashankar, M.A. Alzohairy, A. Almatroudi, M.N. Alomary, S.M.M. Asiri, B.S. Ashwini, N.K. Kalagatur, C. S. Nayak, S.R. Niranjana, Biofabrication of zinc oxide nanoparticles from Melia azedarach and its potential in controlling soybean seed-borne phytopathogenic fungi, Saudi J. Biol. Sci. 27 (2020) 1923–1930, https://doi.org/10.1016/j.sjbs.2020.06.013.
[36] A.K. Shimi, C. Parvathiraj, S. Kumari, J. Dalal, V. Kumar, S.M. Wabaidur, Z. Alothman, Green synthesis of SrO nanoparticles using leaf extract of Albizia julibrissin and its recyclable photocatalytic activity: an eco-friendly approach for treatment of industrial wastewater, Environ. Sci. Adv. 1 (2022) 849–861, https://doi.org/10.1039/d2va00018k.
[37] P. Rajaram, A.R. Jeice, K. Jayakumar, Review of green synthesized TiO2 nanoparticles for diverse applications, Surf. Interfaces 39 (2023) 102912, https://doi.org/10.1016/j.surfin.2023.102912.
[38] M. Naseer, U. Aslam, B. Khalid, B. Chen, Green route to synthesize zinc oxide nanoparticles using leaf extracts of Cassia fistula and Melia azadarach and their antibacterial potential, Sci. Rep. 10 (2020) 1–10, https://doi.org/10.1038/s41598-020-65949-3.
[39] E. Dinga, D.M.N. Mthiyane, U. Marume, T.L. Botha, S. Horn, R. Pieters, V. Wepener, A. Ekennia, D.C. Onwudiwe, Biosynthesis of ZnO nanoparticles using Melia azedarach seed extract: evaluation of the cytotoxic and antimicrobial potency, OpenNano 8 (2022) 100068, https://doi.org/10.1016/j.onano.2022.100068.
[40] A.K. Sidhu, N. Verma, P. Kaushal, Role of biogenic capping agents in the synthesis of metallic nanoparticles and evaluation of their therapeutic potential, Front. Nanotechnol. 3 (2022) 1–17, https://doi.org/10.3389/fnano.2021.801620.
[41] R. Sukirtha, K.M. Priyanka, J.J. Antony, S. Kamalakkannan, R. Thangam, P. Gunasekaran, M. Krishnan, S. Achiraman, Cytotoxic effect of green synthesized silver nanoparticles using Melia azedarach against in vitro HeLa cell lines and lymphoma mice model, Process Biochem. 47 (2012) 273–279, https://doi.org/10.1016/j.procbio.2011.11.003.
[42] A.K. Mittal, Y. Chisti, U.C. Banerjee, Synthesis of metallic nanoparticles using plant extracts, Biotechnol. Adv. 31 (2013) 346–356, https://doi.org/10.1016/j.biotechadv.2013.01.003.
[43] K. Vijayaraghavan, T. Ashokkumar, Plant-mediated biosynthesis of metallic nanoparticles: a review of literature, factors affecting synthesis, characterization techniques and applications, J. Environ. Chem. Eng. 5 (2017) 4866–4883, https://doi.org/10.1016/j.jece.2017.09.026.
[44] N. Nazar, I. Bibi, S. Kamal, M. Iqbal, S. Nouren, K. Jilani, M. Umair, S. Ata, Cu nanoparticles synthesis using biological molecule of P. granatum seeds extract as reducing and capping agent: Growth mechanism and photo-catalytic activity, Int. J. Biol. Macromol. 106 (2018) 1203–1210, https://doi.org/10.1016/j.ijbiomac.2017.08.126.
[45] M. Dadkhah, J.M. Tulliani, Green synthesis of metal oxides semiconductors for gas sensing applications, Sensors 22 (2022) 4669, https://doi.org/10.3390/s22134669.
[46] S.M. Mahdi Ismail, S.M. Ahmed, A.F. Abdulrahman, M.A. AlMessiere, Characterization of green synthesized of ZnO nanoparticles by using Pinus brutia leaves extracts, J. Mol. Struct. 1280 (2023) 135063, https://doi.org/10.1016/j.molstruc.2023.135063.
[47] T. Karnan, S.A.S. Selvakumar, Biosynthesis of ZnO nanoparticles using rambutan (Nephelium lappaceumL.) peel extract and their photocatalytic activity on methyl orange dye, J. Mol. Struct. 1125 (2016) 358–365, https://doi.org/10.1016/j.molstruc.2016.07.029.
[48] A.A. Kashale, K.P. Gattu, K. Ghule, V.H. Ingole, S. Dhanayat, R. Sharma, J. Y. Chang, A.V. Ghule, Biomediated green synthesis of TiO2 nanoparticles for lithium ion battery application, Compos. Part B Eng. 99 (2016) 297–304, https://doi.org/10.1016/j.compositesb.2016.06.015.
[49] Udayabhanu, G. Nagaraju, H. Nagabhushana, D. Suresh, C. Anupama, G.K. Raghu, S.C. Sharma, Vitis labruska skin extract assisted green synthesis of ZnO super structures for multifunctional applications, Ceram. Int. 43 (2017) 11656–11667, https://doi.org/10.1016/j.ceramint.2017.05.351.
[50] M. Rafique, J. Jahangir, B.A.Z. Amin, M. Bilal Tahir, G. Nabi, M. Isa Khan, N. R. Khalid, S.S.A. Gillani, I. Sadaf, Investigation of photocatalytic and seed germination effects of TiO2 nanoparticles synthesized by Melia azedarach L. leaf extract, J. Inorg. Organomet. Polym. Mater. 29 (2019) 2133–2144, https://doi.org/10.1007/s10904-019-01173-5.
[51] K.V. Dhandapani, D. Anbumani, A.D. Gandhi, P. Annamalai, B. S. Muthuvenkatachalam, P. Kavitha, B. Ranganathan, Green route for the synthesis of zinc oxide nanoparticles from Melia azedarach leaf extract and evaluation of their antioxidant and antibacterial activities, Biocatal. Agric. Biotechnol. 24 (2020) 101517, https://doi.org/10.1016/j.bcab.2020.101517.
[52] E.T. Helmy, E.M. Abouellef, U.A. Soliman, J.H. Pan, Novel green synthesis of S-doped TiO2 nanoparticles using Malva parviflora plant extract and their photocatalytic, antimicrobial and antioxidant activities under sunlight illumination, Chemosphere 271 (2021) 129524, https://doi.org/10.1016/j.chemosphere.2020.129524.
[53] R. Senthamarai, V. Madurai Ramakrishnan, B. Palanisamy, S. Kulandhaivel, Synthesis of TiO2 nanostructures by green approach as photoanodes for dye-sensitized solar cells, Int. J. Energy Res. 45 (2021) 3089–3096, https://doi.org/10.1002/er.6002.
[54] I. Paramasivam, J.M. Macak, T. Selvam, P. Schmuki, Electrochemical synthesis of self-organized TiO2 nanotubular structures using an ionic liquid (BMIM-BF4),

Electrochim. Acta 54 (2008) 643–648, https://doi.org/10.1016/J.ELECTACTA.2008.07.031.
[55] R.M. Fernández-Domene, R. Sánchez-Tovar, B. Lucas-Granados, G. Roselló-Márquez, J. García-Antón, A simple method to fabricate high-performance nanostructured WO3 photocatalysts with adjusted morphology in the presence of complexing agents, Mater. Des. 116 (2017) 160–170, https://doi.org/10.1016/j.matdes.2016.12.016.
[56] S.A. Batool, M. Salman Maqbool, M.A. Javed, A. Niaz, M.A.U. Rehman, A review on the fabrication and characterization of titania nanotubes obtained via electrochemical anodization, Surfaces 5 (2022) 456–480, https://doi.org/10.3390/surfaces5040033.
[57] H. Aoudia, B.D. Oomah, F. Zaidi, R. Zaidi-Yahiaoui, J.C.G. Drover, J.E. Harrison, Phenolics, antioxidant and anti-inflammatory activities of Melia azedarach extracts, Int. J. Appl. Res. Nat. Prod. 6 (2013) 19–29.
[58] S. Kuppusamy, P. Thavamani, M. Megharaj, R. Nirola, Y.B. Lee, R. Naidu, Assessment of antioxidant activity, minerals, phenols and flavonoid contents of common plant/tree waste extracts, Ind. Crops Prod. 83 (2016) 630–634, https://doi.org/10.1016/j.indcrop.2015.12.060.
[59] Y. M'rabet, N. Rokbeni, S. Cluzet, A. Boulila, T. Richard, S. Krisa, L. Marzouki, H. Casabianca, K. Hosni, Profiling of phenolic compounds and antioxidant activity of Melia azedarach L. leaves and fruits at two stages of maturity, Ind. Crops Prod. 107 (2017) 232–243, https://doi.org/10.1016/j.indcrop.2017.05.048.
[60] Y.F. Galata, Y.E. Arslan, B. Efe, Assessment of the cytotoxicity of Melia azedarach L. extracts on human adipose-derived mesenchymal stem cells, Hacet. J. Biol. Chem. 1 (2018) 121–128, https://doi.org/10.15671/hjbc.2018.220.
[61] G. Roselló-Márquez, R.M. Fernández-Domene, R. Sánchez-Tovar, J. García-Antón, Photoelectrocatalyzed degradation of organophosphorus pesticide fenamiphos using WO3 nanorods as photoanode, Chemosphere 246 (2020) 1–9, https://doi.org/10.1016/j.chemosphere.2019.125677.
[62] M.D. Gernon, M. Wu, T. Buszta, P. Janney, Environmental benefits of methanesulfonic acid: comparative properties and advantages, Green. Chem. 1 (1999) 127–140, https://doi.org/10.1039/a900157c.
[63] K. Binnemans, P.T. Jones, Methanesulfonic acid (MSA) in hydrometallurgy, J. Sustain. Metall. 9 (2023) 26–45, https://doi.org/10.1007/s40831-022-00641-6.
[64] A. Di Paola, F. Di Quarto, C. Sunseri, Anodic oxide films on tungsten-I. The influence of anodizing parameters on charging curves and film composition, Corros. Sci. 20 (1980) 1067–1078, https://doi.org/10.1016/0010-938X(80)90085-2.
[65] C. Ng, C. Ye, Y.H. Ng, R. Amal, Flower-shaped tungsten oxide with inorganic fullerene-like structure: synthesis and characterization, Cryst. Growth Des. 10 (2010) 3794–3801, https://doi.org/10.1021/cg100625m.
[66] J. Zeng, R.J. Ma, L. Wang, S.N. Zhang, H.Z. Song, Y. Yang, Q.G. Tan, Chemical constituents from the leaves of Melia azedarach, Nat. Prod. Res. 33 (2019) 2860–2863, https://doi.org/10.1080/14786419.2018.1501690.
[67] R.C. Hider, Z.D. Liu, H.H. Khodr, Metal chelation of polyphenols, Methods Enzymol. 335 (2001) 190–203, https://doi.org/10.1016/S0076-6879(01)35243-6.
[68] L. Malacaria, J. Bijlsma, R. Hilgers, W.J.C. de Bruijn, J.P. Vincken, E. Furia, Insights into the complexation and oxidation of quercetin and luteolin in aqueous solutions in presence of selected metal cations, J. Mol. Liq. 369 (2023) 120840, https://doi.org/10.1016/j.molliq.2022.120840.
[69] S.B. Upadhyay, R.K. Mishra, P.P. Sahay, Enhanced acetone response in co-precipitated WO3 nanostructures upon indium doping, Sens. Actuators B Chem. 209 (2015) 368–376, https://doi.org/10.1016/j.snb.2014.11.138.
[70] A.A. Keshk, A. Abu-Rayyan, N.H. Elsayed, M. Al-Anazi, S. Said, N.A. Alamrani, R. M. El-Shabasy, K.R. Shoueir, Adsorption/photocatalytic and antibacterial insole of chitosan-stabilized tungsten trioxide nanosheets, Biomass Convers. Biorefin. (2023), https://doi.org/10.1007/s13399-023-04168-y.
[71] A. Priya, R.A. Senthil, A. Selvi, P. Arunachalam, C.K. Senthil Kumar, J. Madhavan, R. Boddula, R. Pothu, A.M. Al-Mayouf, A study of photocatalytic and photoelectrochemical activity of as-synthesized WO3/g-C3N4 composite photocatalysts for AO7 degradation, Mater. Sci. Energy Technol. 3 (2020) 43–50, https://doi.org/10.1016/j.mset.2019.09.013.
[72] H.H. Afify, S.A. Hassan, M. Obaida, I. Moussa, A. Abouelsayed, Preparation, characterization, and optical spectroscopic studies of nanocrystalline tungsten oxide WO3, Opt. Laser Technol. 111 (2019) 604–611, https://doi.org/10.1016/j.optlastec.2018.10.036.
[73] M.B. Tahir, G. Nabi, N.R. Khalid, Enhanced photocatalytic performance of visible-light active graphene-WO3 nanostructures for hydrogen production, Mater. Sci. Semicond. Process. 84 (2018) 36–41, https://doi.org/10.1016/j.mssp.2018.05.006.
[74] R.M. Fernández-Domene, R. Sánchez-Tovar, B. Lucas-granados, M.J. Muñoz-Portero, J. García-Antón, Elimination of pesticide atrazine by photoelectrocatalysis using a photoanode based on WO3 nanosheets, Chem. Eng. J. 350 (2018) 1114–1124, https://doi.org/10.1016/j.cej.2018.06.015.
[75] F. Amano, M. Tian, B. Ohtani, A. Chen, Photoelectrochemical properties of tungsten trioxide thin film electrodes prepared from facet-controlled rectangular platelets, J. Solid State Electrochem. 16 (2012) 1965–1973, https://doi.org/10.1007/s10008-011-1586-2.
[76] M. Yagi, S. Maruyama, K. Sone, K. Nagai, T. Norimatsu, Preparation and photoelectrocatalytic activity of a nano-structured WO3 platelet film, J. Solid State Chem. 181 (2008) 175–182, https://doi.org/10.1016/j.jssc.2007.11.018.
[77] M. Miyauchi, Photocatalysis and photoinduced hydrophilicity of WO3 thin films with underlying Pt nanoparticles, Phys. Chem. Chem. Phys. 10 (2008) 6258–6265, https://doi.org/10.1039/b807426g.
[78] O. Hurtado-Aular, R. Añez, A. Sierraalta, DFT+U study of the electronic structure changes of WO3 monoclinic and hexagonal surfaces upon Cu, Ag, and Au adsorption. Applications for CO adsorption, Surf. Sci. 714 (2021), https://doi.org/10.1016/j.susc.2021.121907.
[79] P. Li, X. Li, Z. Zhao, M. Wang, T. Fox, Q. Zhang, Y. Zhou, Correlations among structure, composition and electrochemical performances of WO3 anode materials for lithium ion batteries, Electrochim. Acta 192 (2016) 148–157, https://doi.org/10.1016/j.electacta.2016.01.199.
[80] X. Dong, Y. Liu, S. Zhu, Y. Ou, X. Zhang, W. Lan, H. Guo, C. Zhang, Z. Liu, S. Ju, Y. Miao, Y. Zhang, H. Li, Architecting hierarchical WO3 agglomerates assembled with straight and parallel aligned nanoribbons enabling high capacity and robust stability of lithium storage, Front. Chem. 9 (2022) 1–9, https://doi.org/10.3389/fchem.2021.834418.
[81] Y. Zhang, K. Zhu, R. Li, S. Zeng, L. Wang, Structural construction of WO3 nanorods as anode materials for lithium-ion batteries to improve their electrochemical performance, Nanomaterials 13 (2023) 776, https://doi.org/10.3390/nano13040776.
[82] S. Yoon, C. Jo, S.Y. Noh, C.W. Lee, J.H. Song, J. Lee, Development of a high-performance anode for lithium ion batteries using novel ordered mesoporous tungsten oxide materials with high electrical conductivity, Phys. Chem. Chem. Phys. 13 (2011) 11060–11066, https://doi.org/10.1039/c1cp20940j.
[83] S.K. Park, H.J. Lee, M.H. Lee, H.S. Park, Hierarchically structured reduced graphene oxide/WO3 frameworks for an application into lithium ion battery anodes, Chem. Eng. J. 281 (2015) 724–729, https://doi.org/10.1016/j.cej.2015.07.009.
[84] J. Yin, H. Cao, J. Zhang, M. Qu, Z. Zhou, Synthesis and applications of γ-tungsten oxide hierarchical nanostructures, Cryst. Growth Des. 13 (2013) 759–769, https://doi.org/10.1021/cg301469u.
[85] Y. Liu, Y. Jiao, H. Zhou, X. Yu, F. Qu, X. Wu, Rational design of WO3 nanostructures as the anode materials for lithium-ion batteries with enhanced electrochemical performance, Nano-Micro Lett. 7 (2015) 12–16, https://doi.org/10.1007/s40820-014-0013-5.